SUPPLEMENTAL MATERIAL

Ackerman et al., https://doi.org/10.1084/jem.20161714

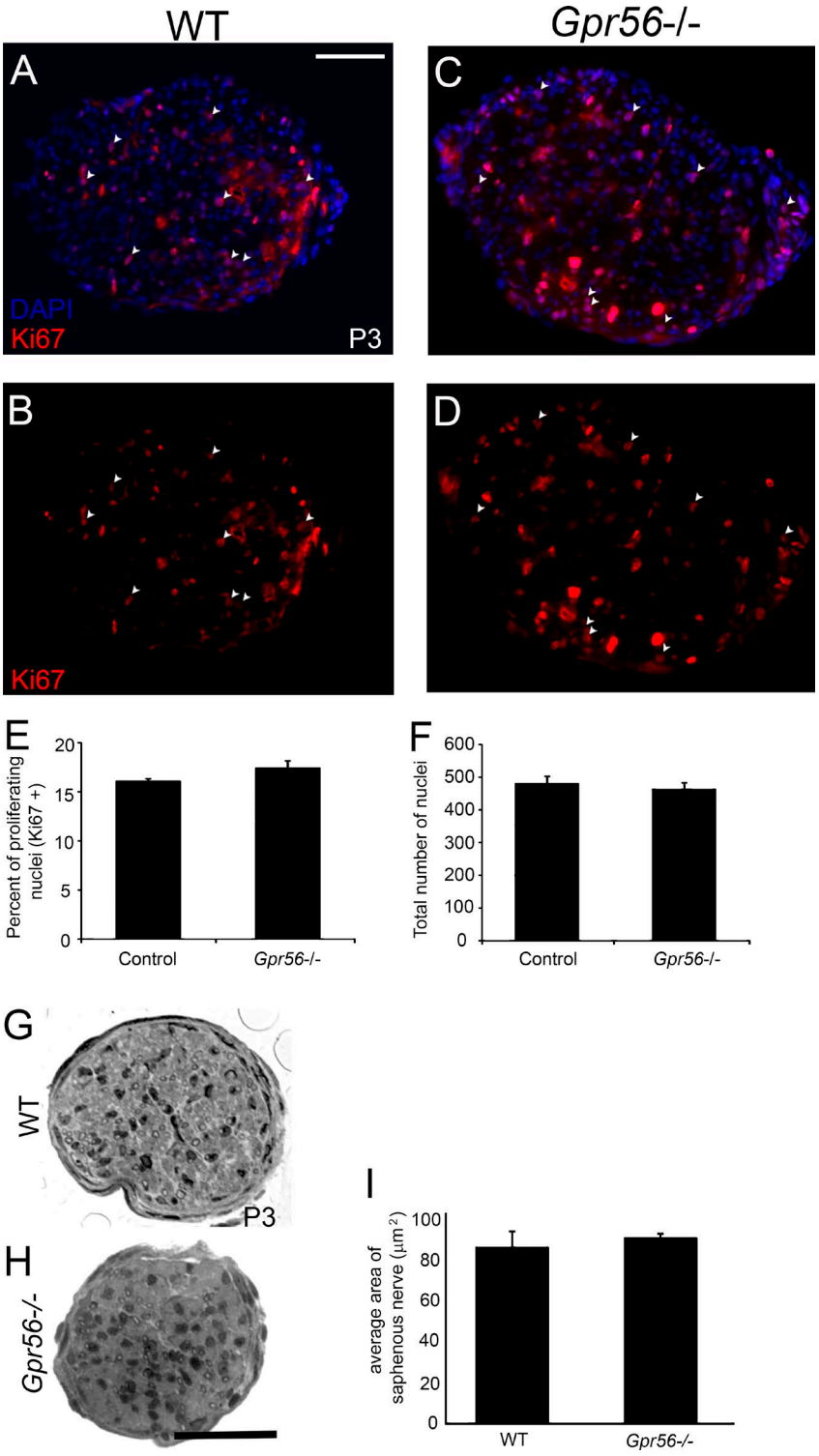

Figure S1. **SC proliferation, number, and nerve size are unaffected in *Gpr56* mouse mutants. (A–D)** IHC on P3 SNs from control (WT and $Gpr56^{+/-}$, $n = 5$) and $Gpr56^{-/-}$ ($n = 3$) animals with DAPI (blue) to mark all nuclei and Ki67 (red) to mark proliferating nuclei. Bar, 50 µm. (B and D) Ki67 stain alone. **(E)** Quantification of the percentage of proliferating nuclei (Ki67+, white arrows) and **(F)** total number of nuclei revealed no significant difference between control (WT and $Gpr56^{+/-}$) and $Gpr56^{-/-}$ nerves. (E) $P < 0.22$, unpaired Student's *t* test. (F) $P < 0.63$, unpaired Student's *t* test. **(G and H)** Representative toluidine blue stains of P3 saphenous nerve from (G) WT ($n = 4$) and $Gpr56^{-/-}$ ($n = 4$). **(I)** Quantification showed no significant difference in saphenous nerve size (area) between WT and mutant ($P < 0.64$, one-way ANOVA). Bar, 40 µm. Error bars represent SEM.

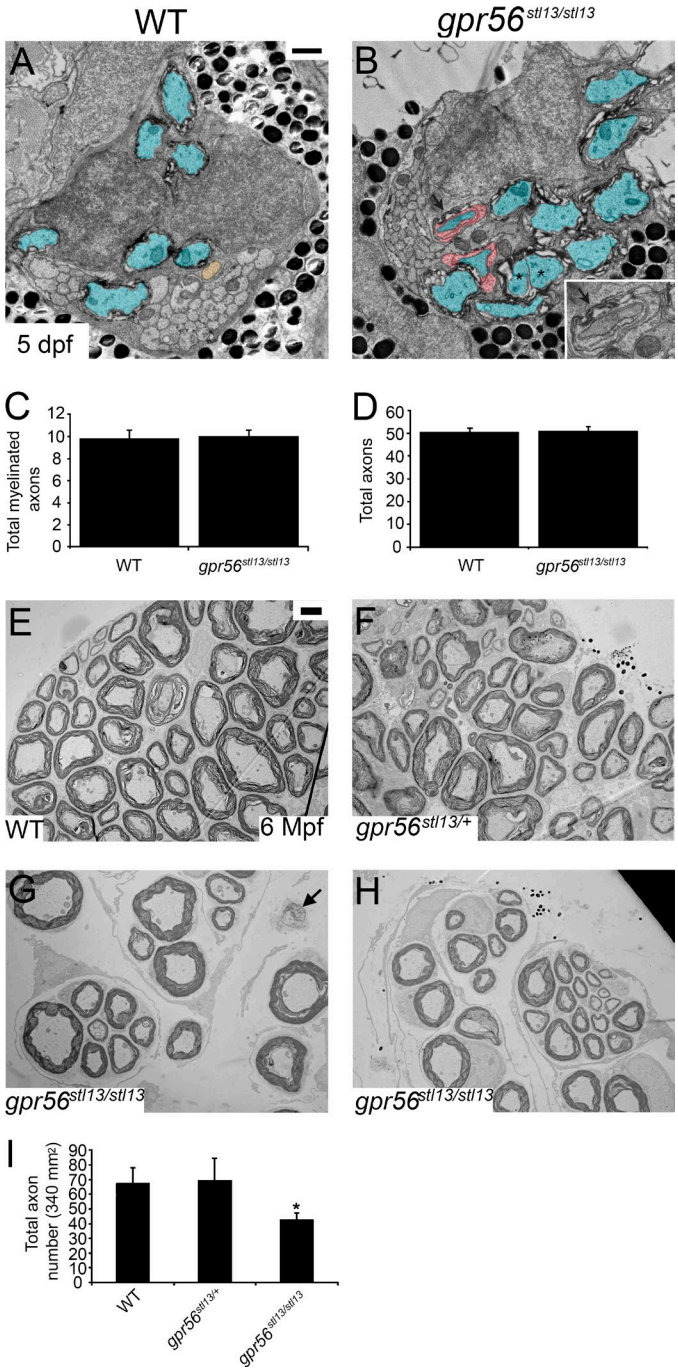

Figure S2. **Gpr56 is required for proper myelin ultrastructure and maintenance in zebrafish. (A and B)** TEM images of the pLLn from (A) WT ($n = 4$) and (B) *gpr56*$^{stl13/stl13}$ mutants ($n = 3$) at 5 dpf. Sorted axons are pseudocolored orange. Sorted and myelinated axons are pseudocolored blue. Bar, 1 µm. (B) Abnormal pockets of SC cytoplasm surrounding mature myelin (pseudocolored red, black arrow) were observed in *gpr56*$^{stl13/stl13}$ nerves and never observed in WT control nerves. The myelinated axon demarcated by the arrow is shown magnified and without pseudocolor in B inset. In addition, myelin wraps encompassing more than one axon (asterisks) were also observed in *gpr56*$^{stl13/stl13}$ mutant nerves ($n = 5/6$ nerves from three of three animals) and never observed in WT ($n = 0/7$ nerves from four of four animals). **(C)** The total number of myelinated axons is unchanged in *gpr56*$^{stl13/stl13}$ mutants by 5 dpf ($P < 0.88$, unpaired Student's *t* test), and **(D)** the total axon number remained unaffected ($P < 0.89$, unpaired Student's *t* test). With age, *gpr56*$^{stl13/stl13}$ mutant nerves exhibit increased myelin defects. Error bars represent SEM. **(E–H)** TEM images of the pLLn from (E) WT, (F) *gpr56*$^{stl13/+}$, and (G and H) *gpr56*$^{stl13/stl13}$ zebrafish ($n = 3$ animals per genotype) at 6 mo postfertilization (Mpf). Bar, 2 µm. (G and H) Nodes of Ranvier (black arrow) and minifascicles were also observed in *gpr56*$^{stl13/stl13}$ nerves but not in WT nerves. **(I)** Quantification of axon number in *gpr56*$^{stl13/stl13}$ mutant nerves revealed a significant decrease in axon number (*, $P < 0.034$) compared with WT controls. Unpaired Student's *t* test was used to test for statistical significance. Error bars represent SEM.

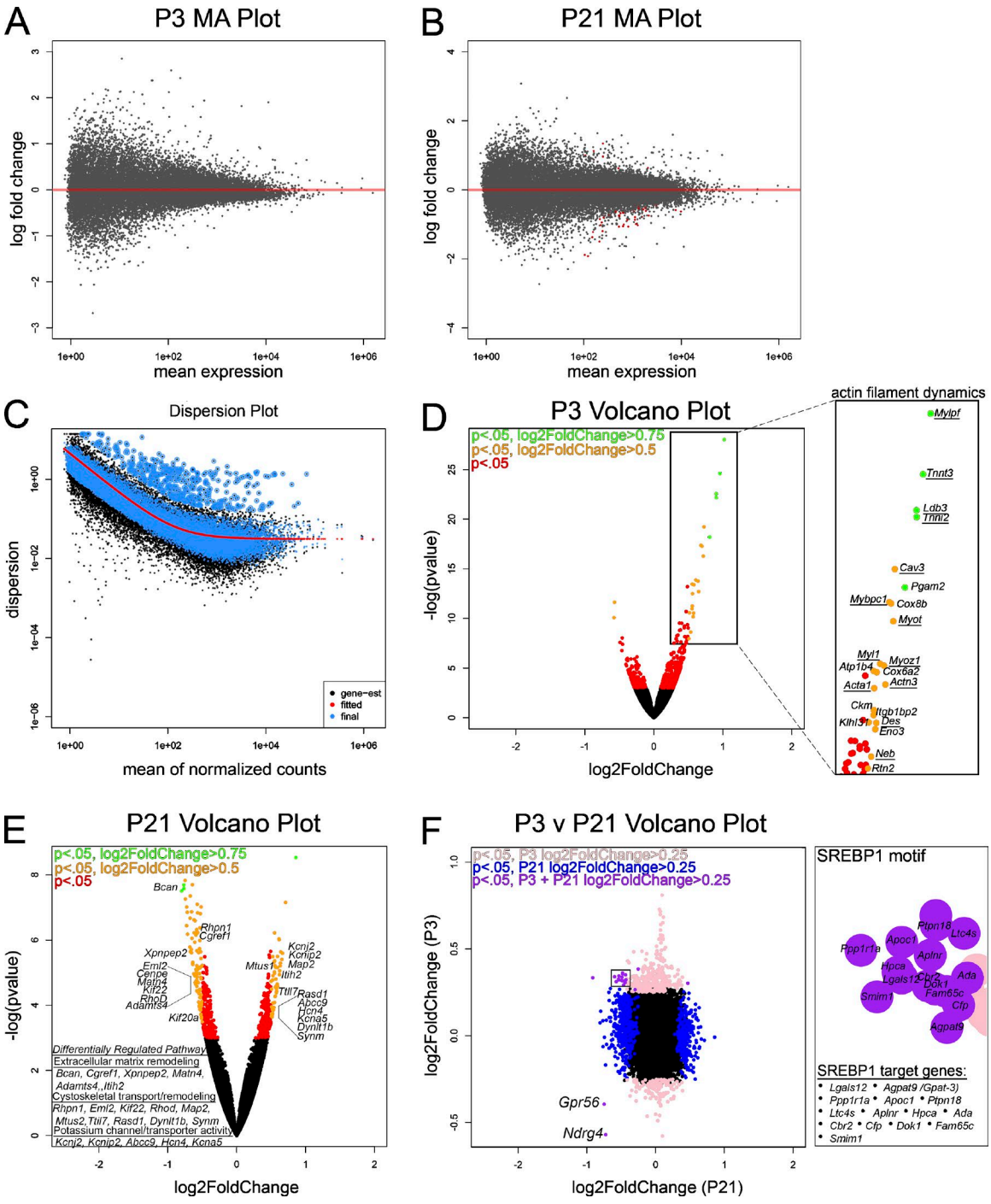

Figure S3. **RNA-seq analysis of *Gpr56* mutant peripheral nerves. (A and B)** MA plots to show the distribution of expression between WT and mutant samples on P3 and P21, respectively ($n = 4$ animals per genotype on P3; $n = 3$ animals per genotype on P21). **(C)** Dispersion plot to show how the data were corrected before analysis to account for variability between replicates ($n = 2$ nerves from one animal per replicate). **(D)** Volcano plot to show differentially expressed genes between *Gpr56* mutant and WT control nerves on P3. Genes that encode modulators of the actin-myosin cytoskeleton are significantly enriched in the mutant sample (right, underline). **(E)** Volcano plot to show differentially expressed genes between mutant and WT on P21. Differentially regulated pathways included (1) extracellular matrix remodeling, (2) cytoskeletal transport/remodeling, and (3) potassium channel/transporter activity. **(F)** Volcano plot to show genes with significant changes in gene expression on P3 alone (pink), genes that were differentially expressed on P21 alone (blue), and shared differentially expressed genes (purple) on P3 and P21. Notably, SREBP1 target genes showed significant differential expression at both time points (right). *Ndrg4*, a gene that is required for sodium channel clustering is significantly down-regulated at both time points. Importantly, *Gpr56* was also significantly down-regulated in mutant nerves at both stage.

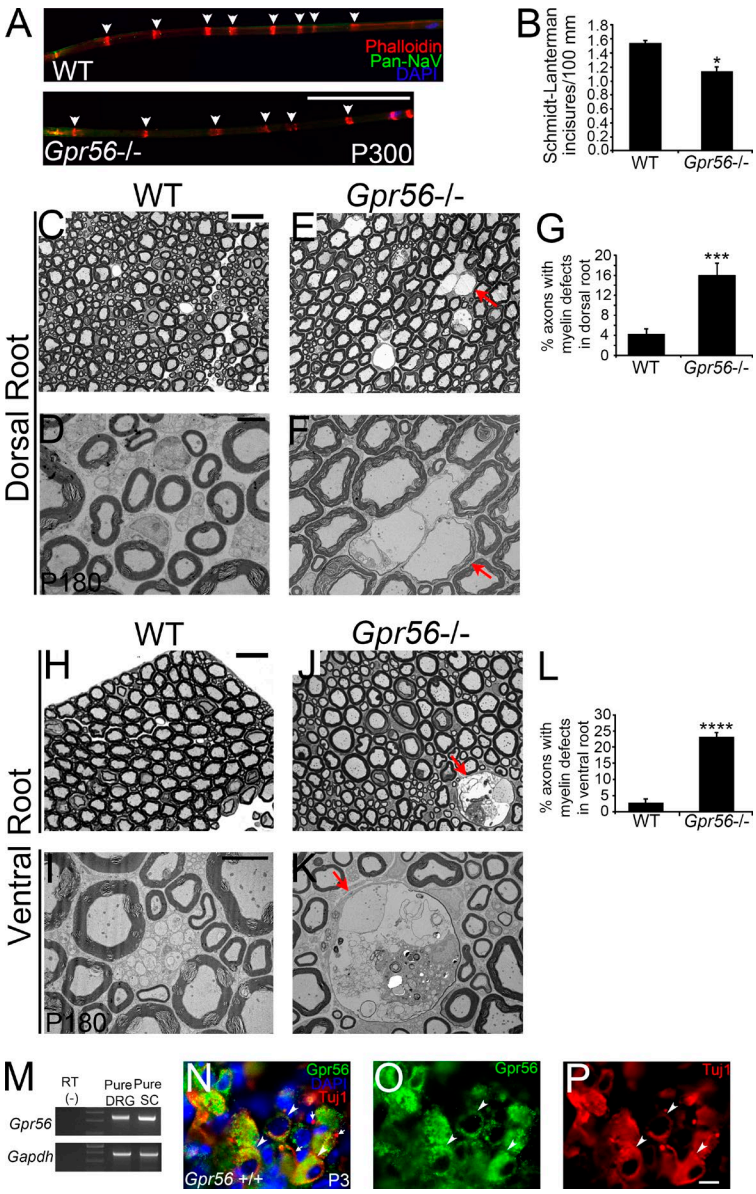

Figure S4. ***Gpr56*$^{-/-}$ mouse dorsal and ventral spinal roots exhibit myelin defects. (A)** IHC showing Phalloidin to mark Schmidt-Lanterman incisures (red, white arrowheads), Pan-NaV (pan sodium channel to mark nodes of Ranvier, green), and DAPI (nuclear stain, blue) localization on teased nerve fibers from WT (top) and *Gpr56*$^{-/-}$ mice on P300 (bottom, $n = 3$ animals per genotype). Bar, 100 µm. **(B)** Quantification of the number of Schmidt-Lanterman incisures per 100 µm of internode revealed a significant decrease in the number of incisures present on mutant fibers compared with control fibers (*, $P < 0.012$). Unpaired Student's *t* test was used to test for statistical significance. Error bars represent SEM. **(C)** Toluidine blue stain of semithin (200 nm) section from WT dorsal root ($n = 2$ animals, two roots each examined) on P180. **(D)** TEM image from WT dorsal root on P180 ($n = 2$ animals, two roots each examined). **(E)** Toluidine blue stain of semithin (200 nm) section from *Gpr56*$^{-/-}$ dorsal root ($n = 2$ animals, two roots each examined) on P180. **(F)** TEM image from *Gpr56*$^{-/-}$ dorsal root on P180 ($n = 3$ animals). Naked axons were present in all dorsal roots examined (red arrow). **(G)** Quantification of the percentage of axons exhibiting myelin defects revealed a significant increase in *Gpr56*$^{-/-}$ dorsal roots (***, $P < 0.001$, one-way ANOVA) compared with WT controls. Error bars represent SEM. **(H)** Toluidine blue stain of semithin (200 nm) section from WT ventral root on P180 ($n = 2$ animals, two roots each examined). **(I)** TEM image from WT ventral root on P180 ($n = 2$ animals, two roots each examined). **(J)** Toluidine blue stain of semithin (200 nm) sections from *Gpr56*$^{-/-}$ ventral root on P180 ($n = 3$ animals). Signs of demyelinated axons are present (red arrow). **(K)** TEM image from *Gpr56*$^{-/-}$ ventral root on P180 ($n = 3$ animals). Demyelinating axons engulfed by macrophages were evident (red arrow). **(L)** There was a significant increase in the percent of axons exhibiting myelin defects in *Gpr56*$^{-/-}$ ventral roots (****, $P < 5.38 \times 10^{-10}$, one-way ANOVA) compared with WT controls. Error bars represent SEM. (M-P) GPR56 is expressed in DRG neurons. (K and L) Bars: (Toluidine blue sections) 20 µm; (TEM sections) 4 µm. **(M)** RT-PCR showing expression of *Gpr56* and *Gapdh* in purified mouse DRG neurons compared with purified rat SCs. Data are representative of two technical replicates. **(N–P)** Representative IHC on P3 DRG showing colocalization of GPR56 (green) with Tuj1 (red) in DRG neuron cell bodies (white arrowheads). DAPI, blue. GPR56 was not readily detected in Tuj1+ axons (white arrows). Three DRGs from three animals assessed for GPR56 expression.

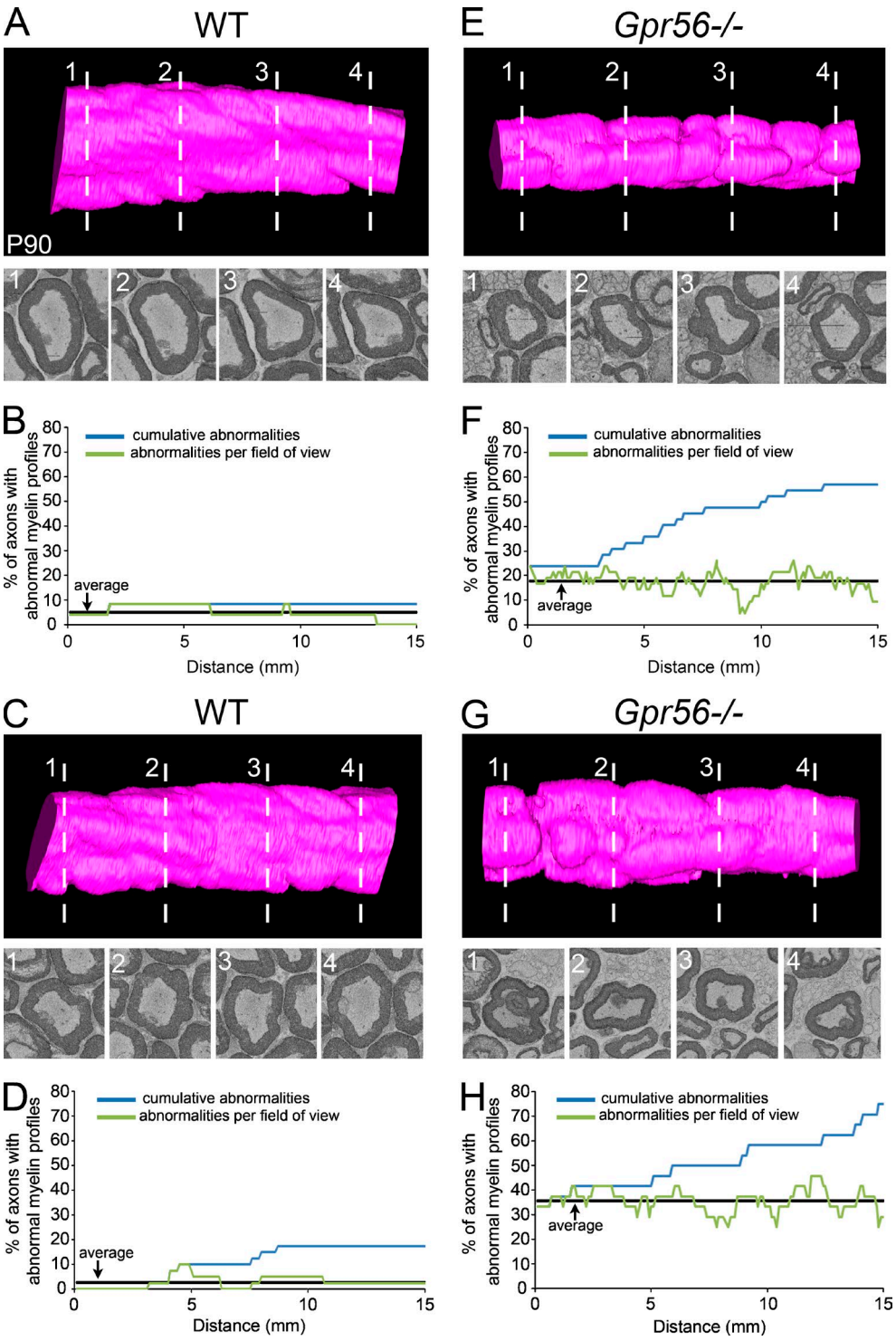

Figure S5. ***Gpr56* is required for mature myelin stability. (A–H)** Serial scanning EM images (350 images, 100 nm apart) of WT (A and C) and *Gpr56*$^{-/-}$ (E and G) SNs on P90 (n = 3 animals per genotype) were acquired and reconstructed to generate the WT and *Gpr56*$^{-/-}$ models shown. Single sections taken from multiple locations along the nerve (1–4) are placed below each model (approximate location denoted by white dashed line). The percentage of axons with abnormal myelin profiles was calculated per section over a 15-µm distance for both WT (B and D) and *Gpr56* mutant (F and H) reconstructions and are graphed to show the percentage of abnormalities per section or field of view (green line), the average percentage of abnormalities given the percentage per section (black line), and the cumulative percentage of abnormalities or the percentage of axons that show at least one abnormality over the 15-µm distance (blue line).

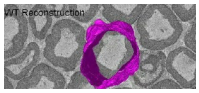

Video 1. **Serial reconstruction of a myelinated fiber from a WT mouse SN on P90.** The video shows construction of a WT model (purple) from 350 successive scanning EM images (100 nm thick).

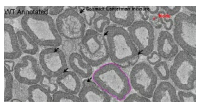

Video 2. **Serial scanning EM images from a WT mouse SN on P90.** The video shows 210 successive sections (100 nm thick) with Schmidt-Lanterman incisures denoted by black arrows and nodes of Ranvier marked by red asterisks.

Video 3. **Serial reconstruction of a myelinated fiber from Gpr56$^{-/-}$ mutant mouse SN on P90.** This video shows the construction of a Gpr56 mutant model (purple) from 350 successive scanning EM images (100 nm thick).

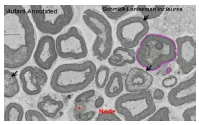

Video 4. **Serial scanning EM images from a Gpr56$^{-/-}$ mutant mouse SN on P90.** This video shows 210 successive sections (100 nm thick) with Schmidt-Lanterman incisures denoted by black arrows and nodes of Ranvier marked by red asterisks.

Dataset 1 presents data about proteins enriched in pseudopods after induction by BDNF/NT-3 neuronal membranes. (A) 141 proteins were found to be more abundant in pseudopods (Ps/CB ratio >2.5) after induction by neuronal membranes (Ps induced/noninduced ratio >1.1). The subcellular localization of each protein was derived from the UniProt subcellular location. (B) Complete protein ontology analysis of the significant canonical pathways in SC pseudopods. 38 pathways are increased after neuronal membrane stimulation as compared with DMEM.

Dataset 2 presents data on MetaCore analysis to uncover differentially regulated pathways using gProfiler. (A–C) Significantly down-regulated GO processes (A), molecular functions (B), and pathway maps (C) in P3 *Gpr56* mutant nerves compared with WT. (D–F) Significantly increased GO processes (D), molecular functions (E), and pathway maps (F) in P3 *Gpr56* mutant nerves compared with WT. (G–I) Significantly down-regulated GO processes (G), molecular functions (H), and pathway maps (I) in P21 *Gpr56* mutant nerves compared with WT. (J–L) Significantly increased GO processes (J), molecular functions (K), and pathway maps (L) in P21 *Gpr56* mutant nerves compared with WT. Raw data files are freely accessible from Zenodo (https://zenodo.org/record/1154250).